Suppressed plasmonic mode coupling for efficient electro-optic lithium niobate modulator

Research Article Vol. 33, No. 18 / 8 Sep 2025 / Optics Express 37784
Optics EXPRESS

Suppressed plasmonic mode coupling for efficient electro-optic lithium niobate modulator

YAN GAO, VICTOR TORRES-COMPANY, AND JOCHEN SCHRÖDER*

Department of Microtechnology and Nanoscience (MC2), Chalmers University of Technology, SE- 41296 Göteborg, Sweden
*jochen.schroeder@chalmers.se

Abstract: Integrated lithium niobate electro-optic (EO) modulators have received strong attention due to the unique material properties of LN, which include low optical loss, high refractive index, and strong Pockels effect. The trade-off between electro-optic bandwidth (BW) and half-wave voltage (V_π) in LN modulators has been widely studied; however, the trade-off between the voltage-length product ($V_\pi \cdot L$) and optical insertion loss (IL) has received less attention. Nevertheless, it is important for efficient EO modulators. The $V_\pi \cdot L$-IL trade-off originates from the balance between the applied electric field intensity and the absorption losses in metallic electrodes, which are both determined by the distance between electrodes and optical waveguides. Here, we find out tha the absorption loss is highly dependent on the electrode width as a result of the mode coupling between the dielectric waveguide and the metal-dielectric plasmonic modes. And we overcome this trade-off by using a special electrode shape that can suppress the mode coupling. As a result, we numerically demonstrate a 5-fold propagation loss reduction (at the same $V_\pi \cdot L$) and a 16% $V_\pi \cdot L$ reduction (at the same loss) compared to a conventional electrode design. We also show that the proposed design does not degrade the frequency response of the modulator, and a more than 50 GHz 3-dB BW can be achieved with an electrode length of 0.8 cm. Our design principle could be used to achieve high-efficiency EO modulators with low insertion loss. Furthermore, the design principle could also be applied to other optical devices with metal-dielectric waveguide structure, such as EO or thermally tuned phase shifters, filters, and optical resonators, to improve their performance.

1. Introduction

Electro-optic (EO) modulators are essential in optical communication, microwave optics, quantum optics and many other EO systems to convert electrical signals into optical signals [1–4]. A typical EO modulator is formed by electrically altering the real part of the refractive index of the waveguide by means of an electro-optic (EO) effect. Lithium niobate (LN) is one of the most advantageous EO materials for high speed and low drive voltage EO modulators. This is due to its unique material properties such as the strong linear EO coefficient, low optical losses, and a high refractive index [5–11]. With the rapid development of the ultra-low-loss integrated LN waveguide platform, on-chip LN EO modulators have attained great research interest in both academia and industry [12–16].

The performance of an integrated LN modulator is generally quantified using various metrics, including extinction ratio (ER), insertion loss (IL), electro-optic bandwidth (BW), linearity, half-wave voltage (V_π), and voltage-length product ($V_\pi \cdot L$) [17,18]. In an LN modulator, the traveling wave electrode is often used to increase the active region length L, and hence to reduce the half-wave drive voltage V_π, which is inversely proportional to L. However, the increased electrode length directly increases the total microwave propagation loss and limits the achievable

#561851 https://doi.org/10.1364/OE.561851
Journal © 2025 Received 11 Mar 2025; revised 29 May 2025; accepted 3 Jul 2025; published 27 Aug 2025

Optics EXPRESS

BW. This BW-V_π limit in the modulator was recently overcome by using the so-called T-shaped segmented electrodes, which are able to significantly reduce RF loss [19–21]. However, the modulation efficiency $V_\pi \cdot L$ has not changed, and a relatively large footprint is still required for a low V_π.

The $V_\pi \cdot L$ in an LN modulator is mainly determined by the strength of the applied electric field within the modulation region. The electric field strength is inversely proportional to the distance (d) between the electrodes and the optical waveguides. Therefore, we need to reduce d to obtain a smaller $V_\pi \cdot L$. The most important contribution to the optical loss in an LN modulator is the absorption loss caused by the nearby metal electrode. This absorption term is very sensitive to d and increases exponentially as d decreases. Given the inherent source of loss, which cannot be simply avoided, there is thus a further trade-off in an LN modulator: $V_\pi \cdot L$ -*IL*. Attempts have been made to overcome this compromise by introducing functional materials into the modulator. In [22], a high-K material is used as the top cladding, which could increase the intensity of the applied electric field around the LN waveguide. In [23], a transparent electrode is combined with a regular metal electrode to reduce the absorption loss caused by the metal electrode. Both works could achieve a small $V_\pi \cdot L$, however, the additional material increases the fabrication complexity and may cause additional optical losses.

In this work, we investigated the absorption loss in a standard partially etched LN traveling wave (TW) modulator and showed that this absorption loss is largely caused by the mode coupling between the optical waveguide mode and surface plasmon polariton (SPP) modes [24,25]. The plasmonic (*pl*) modes are formed in the metal-LN-SiO_2 structure and the mode field is located mainly in the LN region, which makes the *pl* mode feature a very close propagation constant compared with the optical mode in the LN waveguide. Close propagation constants will make it possible to achieve a phase matching condition and lead to a strong mode coupling between optical and *pl* modes. Investigating the coupling effect between optical and *pl* modes, we found that the absorption losses are enhanced/suppressed depending on the phase matching/mismatching conditions between the two modes, which can be easily controlled by the electrode geometry, for example varying the metal width. Taking advantage of this strong dependence, we propose a special shape design to suppress the mode coupling by altering the phase-matching condition. In this way, we numerically demonstrate a new design principle for an LN modulator to break the $V_\pi \cdot L$-*IL* trade-off in LN. As a result, we achieve a 5× loss-reduction (for the same $V_\pi L$) and a reduction of 16% $V_\pi L$ (for the same loss) compared to the conventional rectangular electrode design based on numerical simulation. We believe that our design principle could be useful for the next generation highly efficient, high speed, and low *IL* modulators. In addition, the proposed absorption loss suppression concept could also be introduced for other optical devices with metal-dielectric waveguide structure, such as: EO/thermally tuned phase shifters, filters, and optical resonators to improve their performance.

2. Absorption loss and mode coupling in LN modulator

The presence of metal electrodes in optical modulators introduces absorption losses in adjacent optical waveguides due to the substantial imaginary component of the metal's refractive index. This detrimental effect becomes particularly pronounced in integrated LN modulators owing to their unique electrodes configuration, where the electrodes are placed on top of thin film LN slab. The metal-LN-SiO_2 sandwich structure, as shown in Fig. 1, establishes a plasmonic (*pl*) waveguide [26,27], which supports a family of *pl* modes. The *pl* modes exhibit an effective index (n_{pl}) which is predominantly determined by the LN's material RI, resulting in values comparable to the effective index (n_{op}) of the optical modes in the LN waveguide. As a result, strong mode coupling occurs between these two waveguide systems, enabling significant energy exchange through evanescent-field interactions. This coupled system can be effectively analyzed using simplified coupled mode theory (CMT) with proper consideration of the metal's complex

Optics EXPRESS

refractive index [25,28]. The simplified coupled mode equations in a two-waveguide system with consideration of propagation loss is:

$$\begin{cases} \frac{d\boldsymbol{E}_1}{dz} = i(\gamma_1 \boldsymbol{E}_1 + \kappa \boldsymbol{E}_2), \\ \frac{d\boldsymbol{E}_2}{dz} = i(\gamma_2 \boldsymbol{E}_2 + \kappa \boldsymbol{E}_1), \end{cases} \tag{1}$$

where the γ_1, γ_2 are complex propagation constants for isolated modes in the two waveguides without coupling, and the $\boldsymbol{E}_1$, $\boldsymbol{E}_2$ are the electric field in the optial and *pl* waveguide respectively in the coupled system. The coupling coefficient κ can be obtained by:[29]:

$$\kappa = \frac{1}{4}\sqrt{\frac{\epsilon_0}{\mu_0}} \iint (n^2(x,y) - n_1^2(x,y))\Phi_1^* \Phi_2 dxdy, \tag{2}$$

where $n(x,y)$ and $n_1(x,y)$ are the refractive index distribution for the coupled system and the isolated optical waveguide respectively. The Φ_1 and Φ_2 are the normalized electric field (the mode power is normalized to be 1 W) for isolated modes.

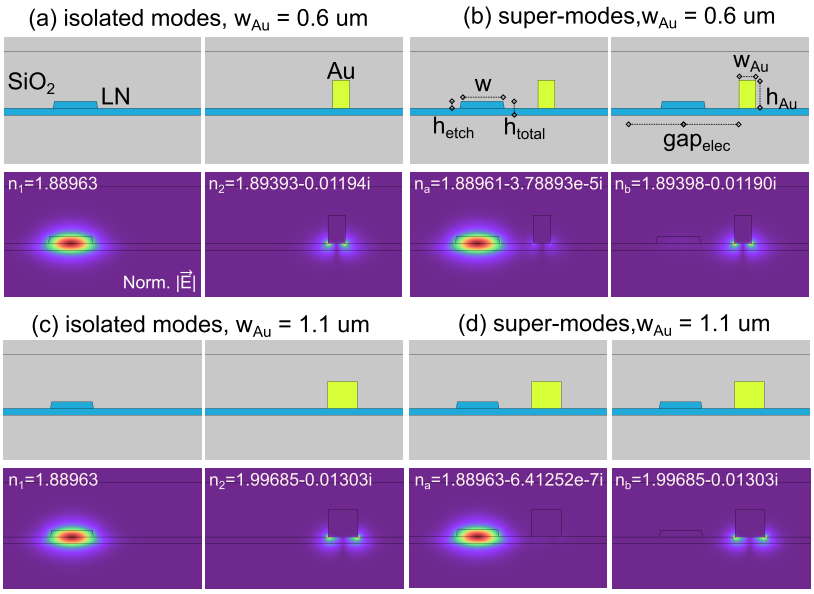

Fig. 1. Diagram of the LN waveguides and electrodes and the corresponding mode profiles for the optical (*op*) and *pl* modes: (a) the isolated modes for metal width of 0.6 μm, (b) for metal width of 1.1 μm; and (c) the coupled super-modes for metal width of 0.6 μm, (d) for metal width of 1.1 μm. In the simulation, the default adaptive triangular meshes are used with a minimum mesh size of 80 nm. The material refractive indices used in the simulation are: n_{LN} = (2.138, 2.21, 2.21), n_{SiO_2} = 1.46, n_{Au} = 0.52 - 10.74i. Parameters used for the simulation are: [h_{total}, h_{etch}, w, w_{Au}, h_{Au}, gap_{elec}] = [0.5, 0.25, 1.5, 0.6, 1, 4] μm.

The mode profiles and propagation constants of the isolated modes and super-modes could be obtained via numerical simulation (Mode solver, COMSOL Multiphyisics). The optical wavelength used in the simulation is 1550 nm. Figure 1 shows the simulated mode profiles for the isolated modes and the coupled super-modes. Figure 1(a) shows the isolated modes profiles for a metal width of 0.6 μm, and the optical mode is nearly phase matched with the *pl* mode (the index difference is 0.0043). In this case, as shown in Fig. 1(b), the two super-modes in the coupled system show different mode profiles compared to the isolated modes, and the mode electric field is partially distributed around the other waveguide. Figure 1(c) shows a similar result for an

Optics EXPRESS

electrode width of 1.1 μm, where the real part of the effective indices are largely different (>0.1) from isolated modes. As shown in the Fig. 1(d), the super modes for such electrodes width show almost the same mode profiles compared with isolated modes, and the mode redistribution around the other waveguide could hardly been seen.

By solving Eq. (1), we could obtain the electric field distribution along the propagation direction, with initial condition: $\boldsymbol{E}_1 = 1$, and $\boldsymbol{E}_2 = 0$ (light input from the optical waveguide). The results are shown in Fig. 2. Here we considered both the lossy case (solid curves in Fig. 2) and the lossless case (dashed curves in Fig. 2). The lossless results are obtained via solving the same coupled mode Eq. (1) by setting the imaginary part of propagation constants (for isolated and coupled modes) to be 0. In Fig. 2(a), the nearly phase matched condition is considered (w_{Au} = 0.6 μm). For the lossless case, the optical power in the optical waveguides will transfer to the *pl* waveguide and then transfer back, and the coupling length L_c is 177 μm (the length for the maximum power transfer to the other waveguide). For the lossy case, the propagation loss in the *pl* mode is around 2102 dB/cm (calculated by the mode complex propagation constant), and the light coupled from optical to *pl* waveguide will be soon dissipated. As a result, the power in the *pl* waveguide first rises up and then decays linearly (the red solid curve in Fig. 2(a)). In optical waveguide, the power first drop down with a nonlinear rate and soon shows a linear decay trend. It's worth to mention that the power decay rates in the linear region for optical and *pl* waveguides are the same and the corresponding propagation loss is around 6 dB/cm. And the loss is close to the propagation loss derived from the complex effective index n_a of the super mode *a*, which is 6.4 dB/cm. For the phase mismatched case (w_{Au} =1.1 μm), as shown in Fig. 2(b), the power evolution in the lossless system is quite similar to the near phase matched case, except that the maximum power transfer ratio is much smaller than that in the Fig. 2(a). In the lossy case, the power in the *pl* waveguide features a small oscillation and then slowly decays linearly. By comparing the power evolution in optical waveguides for both near phase matched and phase

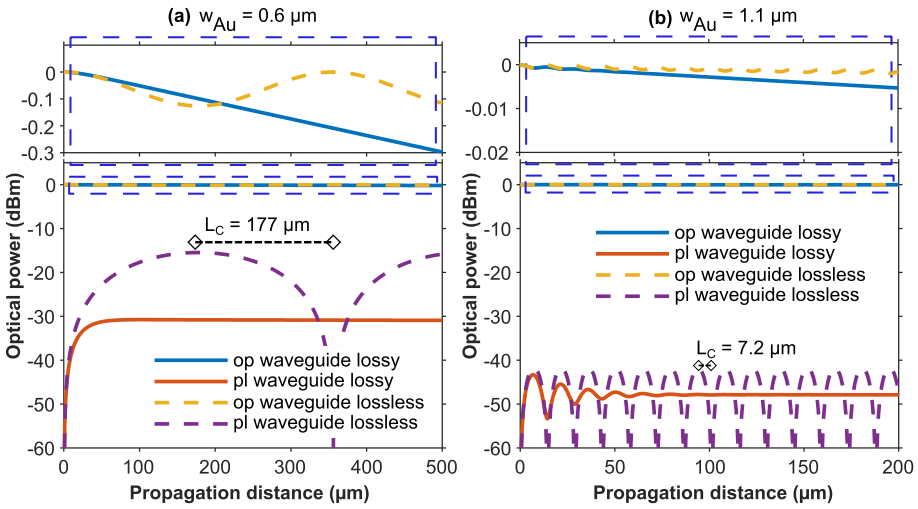

Fig. 2. Calculated optical propagation properties in the two waveguide coupled system based on the CMT: (a) For the metal width of 0.6 μm, and (b) for the metal width of 1.1 μm. Other geometric parameters are the same as in the Fig. 1. The optical input is set to only from the optical waveguide. And the propagation constants used in the CMT calculations are from a finite element method (FEM) simulations based on the mode solver in COMSOL. The solid curves are the calculated results by considering a complex propagation constants - the lossy case, and the dashed curves indicate the lossless case by using a pure real propagation constant.

Optics EXPRESS

mismatched cases, we found the power decay rate in the phase mismatched case is much smaller, which could be explained by the limited maximum power transfer ratio caused by the phase mismatching.

To better understand the power evolution in the propagation direction in the lossy case, we performed a 3D FEM simulations (Beam envelops, COMSOL Multiphyisics) to obtain the electric field distribution along the propagation direction. The waveguides geometric parameters are the same as in the Fig. 1, and the electrode width is 0.6 μm. In the simulation, we first excited one of the eigen modes *a*, *b* (the subscript *a* indicates the mode that located at the optical waveguide and *b* indicates the mode that located at the *pl* waveguide, and the super-modes profiles can be found in Fig. 1(b)). Here the eigen mode aptitude will decrease along propagation due to optical loss and the mode profile will keep the same if there are no perturbations on the waveguide geometry (uniform waveguides). As shown in the Fig. 3(a), (b), the excited eigen mode *b* will decay much faster than the eigen mode *a*. Then we excite both eigen mode *a* and *b* with power ratio of 1:1, as shown in the Fig. 3(c). As expected, the power in the eigen mode *b* will soon be dissipated and the power in the eigen mode *a* is left without significant dissipation. This could help explain the result we obtained from the CMT that the optical loss in the optical waveguide will finally convergence to loss in the super mode *a* (super mode *b* has already been dissipated). According to the above analysis, we will directly use the loss of super mode *a* to represent the propagation loss for the modulator waveguide.

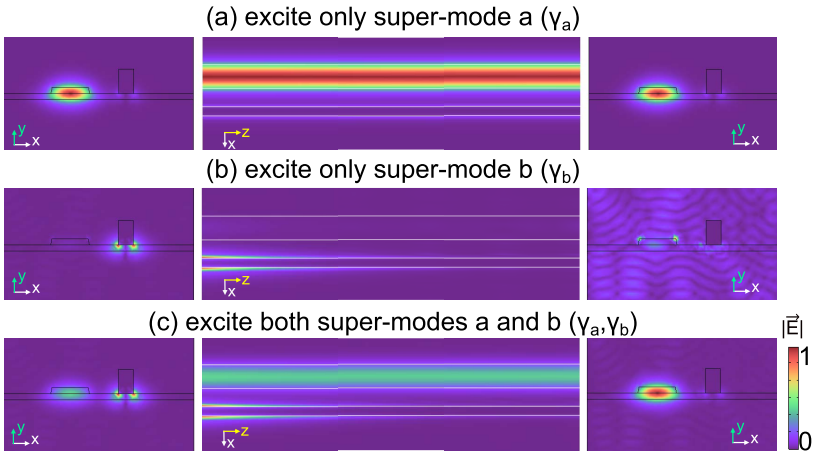

Fig. 3. Simulated propagation properties for the coupled waveguide systems by exciting the corresponding super-modes: (a) excite only super-mode a, with propagation constant, γ_a, (b) excite only super-mode b, with propagation constant, γ_b, and (c) excite both super-modes *a* and *b*, with power ratio of 1:1. The geometric parameters for the waveguide and the electrodes are the same as parameters in Fig 1., the metal width is 0.6 μm, and the propagation length is 60 μm. The output mode profile in (b) is dominated by the background noise.

Next, a quantitative investigation of the optical *pl* mode coupling and the corresponding loss absorption is conducted by using numerical simulations (Mode solver, COMSOL Multiphyisics). As shown in Fig. 4(a), we calculated the real part of the effective index (circular shapes) of the isolated *pl* mode families without optical waveguide. In the simulation, the metal width of the *pl* waveguide is altered and 5 *pl* modes are considered. Similar to an optical mode family, the *pl* modes effective indices are very sensitive to the waveguide width (the metal width here). As a reference, the effective index of the optical mode is also plotted with a constant waveguide width of 1.5 μm. There are a few phase matching points between the two modes, where the real part of the effective index for the two modes are equal to each other. At the matching points, as we

Optics EXPRESS

already discussed, the mode of the dielectric optical waveguide is strongly coupled to one of the metal-dielectric *pl* modes and the optical loss is largely increased due to metal absorption, as shown in Fig. 4(b). Considered in the modulator, one optical waveguide is placed in between two electrodes, the calculated loss is simply doubled by using the optical loss in waveguide with only one electrode. In Fig. 4(b), we can also see a strong dependence of the optical loss on the metal electrode width, which is corresponding to the mode coupling and phase matching condition in the coupled system. If we zoom into the region with an electrode width of about 0-1 μm, we can find a strong absorption peak with a maximum loss of about 12.8 dB/cm (at a metal width of 600 nm), and the minimum loss is only 0.06 dB/cm (at a width of 50 nm). The optical losses have changed by a factor of more than 200. Apart from the absorption areas, there are several other areas where the optical losses are relatively low. In the case of mode coupling, there is a strong wavelength-dependent absorption peak at about 1550 nm (Fig. 4(c)), which leads to large optical losses over a large wavelength range. In the other case, the optical losses remain low (<1 dB/cm)

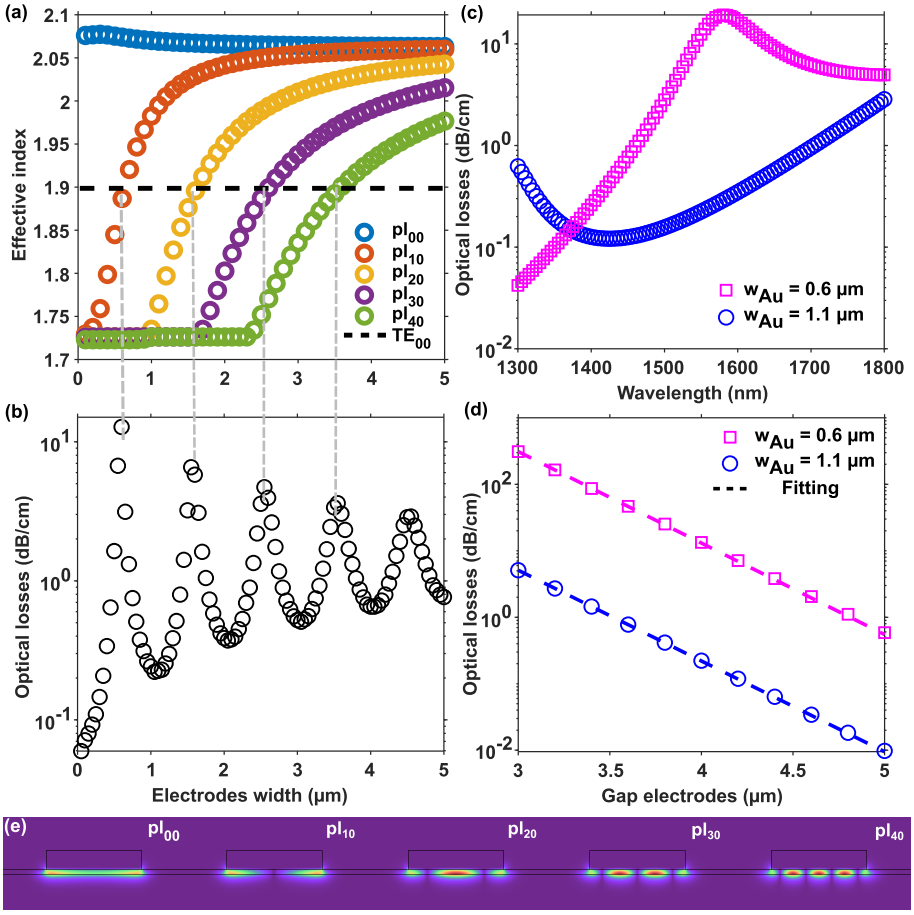

Fig. 4. (a) Real part of the effective index of the *pl* and optical modes with different metal width in a modulator. (b) The corresponding optical losses with different metal width. (b) Calculated optical losses with different wavelength. (d) Calculated optical losses with different electrodes gaps. (e) The simulated mode profiles for the *pl* modes in a 5 μm wide *pl* waveguide. Parameters used in (a)-(b) are: [h_{total}, h_{etch}, w, w_{Au}, h_{Au}, gap_{elec}] = [0.5, 0.25, 1.5, sweep, 1, 4] μm. Parameters in (c)-(d) are the same as in (a)-(b), but chose a certain metal width; and in (c), the electrodes gap is 4 μm, in (d), the gap electrodes is swept.

Optics EXPRESS

over an extremely large wavelength range (> 400 nm). The results show the potential to utilize the effect of mode coupling/mode coupling suppression in wide bandwidth optical components. In addition to the electrode width, the distance between the electrodes has a large influence on optical losses. As can be seen in Fig. 4(d), the trends of the optical losses show an exponential relation to the electrodes gap. To investigate the wavelength sensitivity of the mode coupling, we chose two typical electrode widths: one at strong mode coupling (w_{Au} = 0.6 μm) and one at mode coupling suppression (w_{Au} = 1.1 μm).

3. Electrode shape design for an efficient EO modulator

As mentioned above, the optical absorption loss caused by electrodes is related to the mode coupling and mode profile redistribution, and depends on the width of the electrodes. By choosing an approximate electrode width, we can significantly reduce the absorption loss by suppressing the mode coupling. However, this method cannot be directly used in traveling wave EO modulators because the metal width is determined by the RF design for high frequency operation for the following reasons: velocity matching, low microwave loss and impedance matching. Therefore, the electrode width is usually ten to a few tens of micrometers. As shown in Fig. 4(a), with the increase of electrodes width, the supported mode number increases, and the effective index difference between adjacent modes decreases. As a result, there is a much higher probability in a normal EO modulator, that one or more *pl* modes will match the optical mode with a close effective index.

Figure 5(a) shows a typical mode profile for the waveguide with nearby electrodes, which the mode electric field is partially distributed near the metal region. The mode field redistribution is caused by the mode coupling between optical and one of the high-order *pl* modes. It is worth to emphasize that with a relatively large electrodes width, the absorption loss is much less sensitive to the metal width, as shown in Fig. 5(c). And no matter which metal width it is, there will always be a higher order *pl* mode with a effective index that is close enough to the optical waveguide index and leads to a relatively strong mode coupling.

Here we introduce a supporting dielectric strip, as shown in Fig. 5(b), to break the geometric continuity of the metal-dielectric *pl* interface. Since the *pl* mode is determined by the metal-dielectric interface, the supported modes are significantly changed. Such an electrode shape design splits the *pl* waveguide into two sub-waveguides and the mode coupling from optical to *pl* modes is determined only by the sub-waveguide closer to the optical waveguide. By designing the geometry of the sub-waveguide, we can artificially control the coupling between optical and *pl* modes. Here, the height of the strip is the same as the optical waveguide in order to avoid an additional etching step for the waveguide fabrication. The strip width W_g and the distance between strip edge to the metal edge D_g are determined by parameter optimization to obtain the lowest loss. We have chosen W_g = 1μm and D_g = 1.1 μm. In Fig. 5(b), we show the optical mode profiles in an LN modulator with shape design, where the mode coupling can be suppressed and the mode redistribution is hardly seen.

To further demonstrate how this shape design helps reduce the optical loss, we simulated optical losses in LN modulators with and without shape design over a large range of electrodes width from 0-15 μm. Similar to the previous analysis, the optical losses in a modulator without a shape design depend strongly on the electrode width. However, the optical losses in the modulator with the shape design are largely constant over a large width region. More importantly, the optical propagation losses in the shape-designed modulator (0.28 dB/cm) are reduced significantly, with a more than 5× reduction, compared to the losses in a normal modulator (1.5 dB/cm).

To further quantify the benefit of our design principle in an EO modulator, we calculated both the $V_\pi \cdot L$ and optical losses of a standard modulator without shape design. The DC $V_\pi \cdot L$ is

Optics EXPRESS

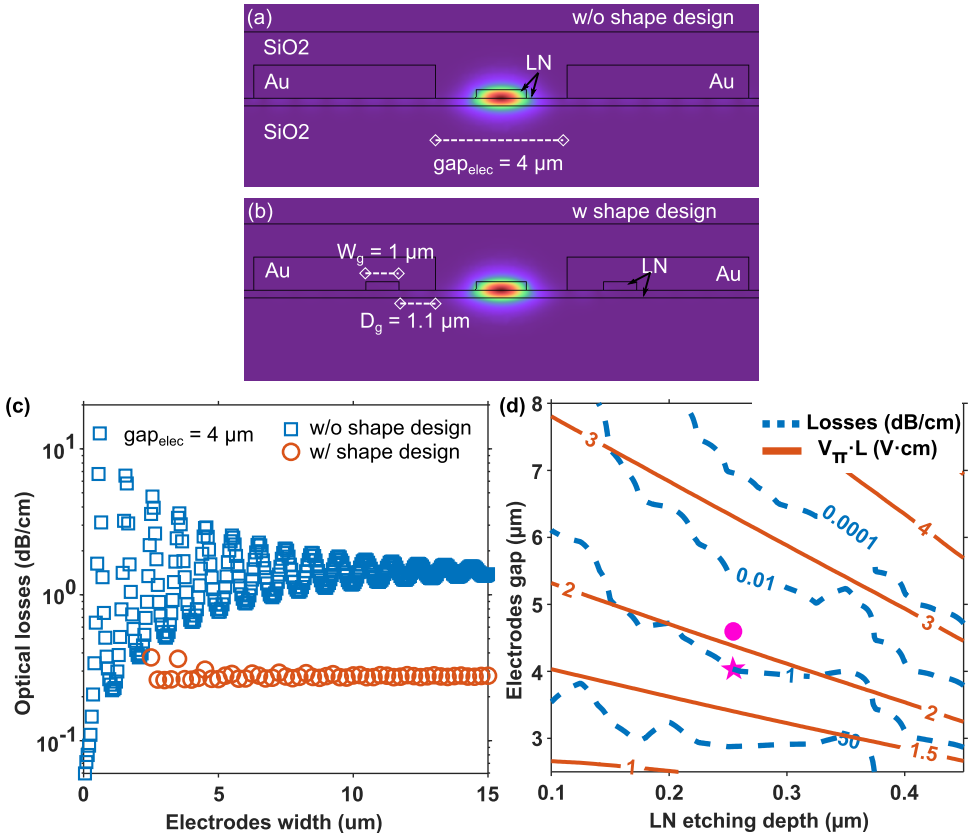

Fig. 5. (a) Optical mode profiles in a standard LN modulator, a strong mode coupling between LN waveguide optical mode and metal-dielectric *pl* modes could be seen. (b) Optical mode profiles in a LN modulator with shape-designed electrodes, the mode coupling is suppressed. (c) Calculated optical losses in modulators with and without electrodes shape design. (d) $V_\pi \cdot L$ and loss optimization with different electrodes gap and LN etching depth, the pink circle indicate the optimized point without shape design and the start indicate the optimized point with the shape design. Parameters used for the simulation are similar to that in the Fig. 1, except the metal width is much wider and w_{Au} = 5 μm. Parameters are listed as: [h_{total}, h_{etch}, w, w_{Au}, h_{Au}, gap_{elec}, W_g, D_g] = [0.5, 0.25, 1.5, 5, 1.15, 4, 1, 1.1] μm.

calculated from the equation:

$$V_\pi L = \frac{\lambda_0 V_0}{\Gamma n_e^3 r_{33}}, \tag{3}$$

where n_e is the extraordinary refractive index of LN, which is 2.13 at 1550 nm. r_{33} = 30.8 pm/V is the strongest EO coefficient of LN crystal. V_0 is the applied voltage to the electrodes. And Γ is the field interaction factor, which can be calculated by:

$$\Gamma = \frac{\iint E_{op}^2(x,y) E_{el}(x,y) dxdy}{\iint E_{op}^2(x,y) dxdy}, \tag{4}$$

where the E_{op}, E_{el} are the optical mode field and the external electric field. Note that E_{el} is the actual electric field without normalization with a DC voltage V_0 applied on the electrodes. The electrode shape does not influence the $V_\pi \cdot L$ of the modulator, and only the gap between the two electrodes and the etching depth of the LN waveguide affect the $V_\pi \cdot L$. As shown in

Optics EXPRESS

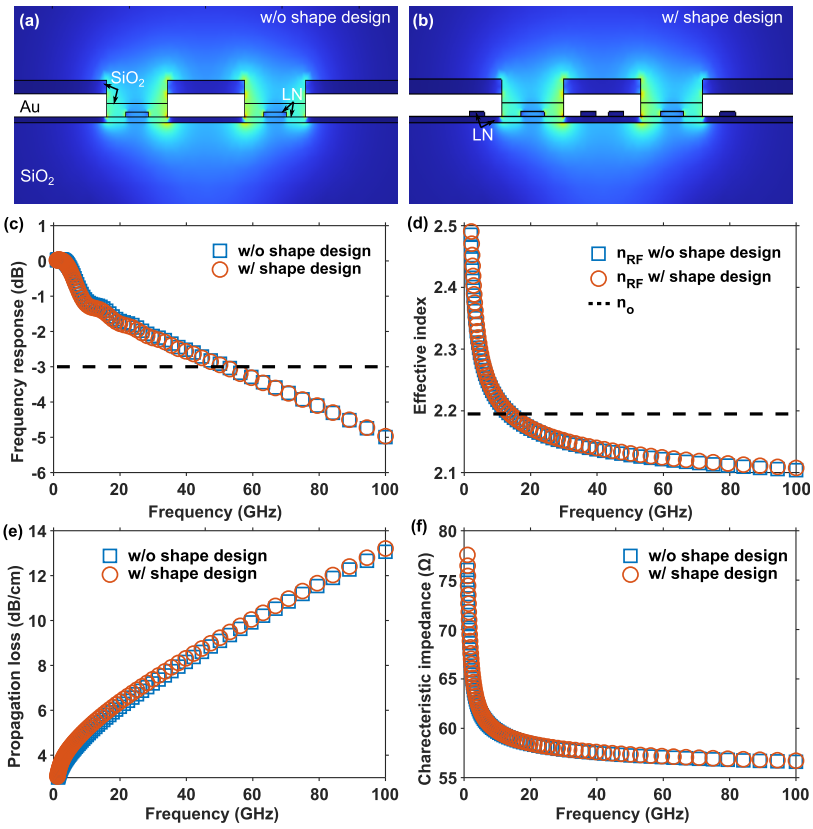

Fig. 6. Simulated RF mode profile (@50 GHz) in the modulator without shape design (a), and with shape design (b). Calculated frequency response (c), RF/optical effective index (d), RF losses (e), and characteristic impedance (f) in modulators without/with electrodes shape design. The geometric parameters used are: [h_{total}, h_{etch}, w, $w_{Au,signal}$, $w_{Au,ground}$, h_{Au}, gap_{elec}, W_g, D_g] = [0.5, 0.25, 1.5, 5, 30, 1.15, 4, 1, 1.1] μm.

Fig. 5(d), the orange curves show the calculated $V_\pi \cdot L$ and the blue curves show the calculated optical losses. Notably, the $V_\pi \cdot L$ product and the propagation loss exhibit opposite trends when modifying the geometric parameters of the modulator, particularly when adjusting the electrode gap. Therefore, for a TW modulator design, it is imperative to optimize the geometric parameters to achieve minimal $V_\pi \cdot L$ while maintaining acceptable waveguide propagation loss. To achieve this objective, we first specify a maximum tolerable propagation loss of 0.2 dB/cm. Subsequent optimization yields a geometry with minimal $V_\pi \cdot L$ (2.1 V·cm) at an etched depth of 250 nm and electrodes gap of 4.6 μm (indicated by the pink dot marker in Fig. 5(d)). Furthermore, implementing the shape design approach enables substantial suppression of propagation loss while retaining identical geometric parameters. This facilitates shifting the optimized operating point under equivalent propagation loss constraints (0.2 dB/cm) to reduced electrodes gaps of 4 μm (denoted by the pink star marker in Fig. 5(d)). As a result, the optimized $V_\pi \cdot L$ is reduced from 2.1 V·cm to 1.76 V·cm, with about 16% reduction, which indicates a more than 30% reduction of energy consumption.

For a TW modulator, another important figure of merit is the EO BW, which can be extracted from the modulator frequency response. In order to obtain a modulator with large BW, we need to consider three important rules: 1) a low RF propagation loss; 2) phase/velocity matching

Optics EXPRESS

between optical wave and RF wave; 3) impedance matching between RF transmission line and the load. The modulator electrode is a coplanar waveguide (CPW) with properties with propagation constant β_{RF}, propagation loss α_{RF} and characteristic impedance Z_0. Once these frequency dependent properties are known, the modulator overall frequency response can be calculated from [30,31]:

$$H(f) = \frac{Z_{in}}{Z_{in} + Z_S} e^{-\alpha_{RF} L/2} \sqrt{\frac{sinh^2(\frac{\alpha_{RF} L}{2}) + sin^2(\frac{\epsilon L}{2})}{(\frac{\alpha_{RF} L}{2})^2 + (\frac{\epsilon L}{2})^2}}, \tag{5}$$

where the $\epsilon = \beta_{RF} - \beta_{op}$, and the β_{op} is the optical propagation constant. The Z_{in} and Z_S are the input (looking from the source) and the source impedance receptively. The CPW electrode is simulated via a 2-D FEM simulation (AC/DC module, COMSOL Multiphyisics). In the simulation, the substrate is silicon, and the simulation region needs to be large enough to avoid simulation errors that come from the RF modes leakage to the substrate. Based on the convergency test, the simulation region is chosen to be 300 × 300 μm. The RF relative dielectric constants used in the simulation are: ϵ_{LN} = (28, 44, 44), with loss tangent of 0.004, ϵ_{sio_2} = 4.2, and ϵ_{Si} = 11.7. As shown in Fig. 6(a), (b), we simulate the electric field of the RF mode with frequency of 50 GHz. And the CPW parameters as well as the modulator frequency response are shown in Fig. 6(c-f). By comparing the results for LN modulator with and without shape design, we do not see any significant differences for high frequency response and the CPW parameters, which indicates the proposed shape design of the electrode will not degrade the modulator BW. As a result, a more than 50 GHz BW LN TW modulator is designed with an electrode length of 0.8 cm.

4. Conclusion

In conclusion, we numerically studied the mode-coupling effect between the dielectric waveguide mode and the metal-dielectric plasmonic mode in a TW LN modulator. We utilized the electrode-width-dependent mode-coupling effect to achieve an efficient LN modulator. We numerically demonstrate that the proposed shape-designed modulator performs better than a standard modulator with rectangular shape, with a 5× propagation loss reduction (with the same $V_\pi L$) or a 16% $V_\pi L$ reduction (with the same loss). We also demonstrated that the shape design does not degrade the frequency response of the modulator, and a BW of more than 50 GHz has been achieved with a 0.8 cm long electrode. Although the efficient modulator design method proposed in this work is developed for a specific LN waveguide with predetermined waveguide parameters, the methodology can be readily extended to more general cases with arbitrary waveguide geometries. This generalization remains valid provided that the mode coupling suppression condition exists within the system. Combined with other start-of-the art design methods, we believe our design method could help to achieve next-generation high-performance EO modulators. Moreover, the mode coupling suppression mechanism investigated in this study can be extended to other waveguide systems, including electro-optic (EO) modulators, thermally tuned phase shifters, wavelength-selective filters, and optical resonators, offering potential performance enhancements in these device architectures.

Funding. Vetenskapsrådet (VR-2017-05157, VR-2021-04241).

Disclosures. The authors declare no conflicts of interest.

Data availability. Data underlying the results presented in this paper are available in Ref. [32].

References

1. E. L. Wooten, K. M. Kissa, A. Yi-Yan, *et al.*, "A review of lithium niobate modulators for fiber-optic communications systems," IEEE J. Select. Topics Quantum Electron. **6**(1), 69–82 (2000).
2. G. T. Reed, G. Mashanovich, F. Y. Gardes, *et al.*, "Silicon optical modulators," Nat. Photonics **4**(8), 518–526 (2010).
3. J. Witzens, "High-speed silicon photonics modulators," Proc. IEEE. **106**(12), 2158–2182 (2018).

Optics EXPRESS

4. M. Howerton, R. Moeller, A. Greenblatt, *et al.*, "Fully packaged, broad-band linbo 3 modulator with low drive voltage," IEEE Photonics Technol. Lett. **12**(7), 792–794 (2000).
5. A. Boes, L. Chang, C. Langrock, *et al.*, "Lithium niobate photonics: Unlocking the electromagnetic spectrum," Science **379**(6627), eabj4396 (2023).
6. D. Zhu, L. Shao, M. Yu, *et al.*, "Integrated photonics on thin-film lithium niobate," Adv. Opt. Photonics **13**(2), 242–352 (2021).
7. M. Zhang, C. Wang, R. Cheng, *et al.*, "Monolithic ultra-high-q lithium niobate microring resonator," Optica **4**(12), 1536–1537 (2017).
8. Y. Gao, F. Lei, M. Girardi, *et al.*, "Compact lithium niobate microring resonators in the ultrahigh q/v regime," Opt. Lett. **48**(15), 3949–3952 (2023).
9. H. Feng, T. Ge, X. Guo, *et al.*, "Integrated lithium niobate microwave photonic processing engine," Nature **627**(8002), 80–87 (2024).
10. J. Lu, A. Al Sayem, Z. Gong, *et al.*, "Ultralow-threshold thin-film lithium niobate optical parametric oscillator," Optica **8**(4), 539–544 (2021).
11. A. Honardoost, K. Abdelsalam, and S. Fathpour, "Rejuvenating a versatile photonic material: thin-film lithium niobate," Laser Photonics Rev. **14**(9), 2000088 (2020).
12. C. Wang, M. Zhang, X. Chen, *et al.*, "Integrated lithium niobate electro-optic modulators operating at cmos-compatible voltages," Nature **562**(7725), 101–104 (2018).
13. M. He, M. Xu, Y. Ren, *et al.*, "High-performance hybrid silicon and lithium niobate mach–zehnder modulators for 100 gbit s- 1 and beyond," Nat. Photonics **13**(5), 359–364 (2019).
14. G. Chen, Y. Gao, H.-L. Lin, *et al.*, "Compact and efficient thin-film lithium niobate modulators," Adv. Photonics Res. **4**(12), 2300229 (2023).
15. M. Zhang, C. Wang, P. Kharel, *et al.*, "Integrated lithium niobate electro-optic modulators: when performance meets scalability," Optica **8**(5), 652–667 (2021).
16. A. Rao, A. Patil, P. Rabiei, *et al.*, "High-performance and linear thin-film lithium niobate mach–zehnder modulators on silicon up to 50 ghz," Opt. Lett. **41**(24), 5700–5703 (2016).
17. G. Sinatkas, T. Christopoulos, O. Tsilipakos, *et al.*, "Electro-optic modulation in integrated photonics," J. Appl. Phys. **130**(1), 010901 (2021).
18. D. A. Miller, "Energy consumption in optical modulators for interconnects," Opt. Express **20**(S2), A293–A308 (2012).
19. S. Sakamoto, R. Spickermann, and N. Dagli, "Narrow gap coplanar slow wave electrode for travelling wave electro-optic modulators," Electron. Lett. **31**(14), 1183–1185 (1995).
20. P. Kharel, C. Reimer, K. Luke, *et al.*, "Breaking voltage–bandwidth limits in integrated lithium niobate modulators using micro-structured electrodes," Optica **8**(3), 357–363 (2021).
21. M. Xu, Y. Zhu, F. Pittalà, *et al.*, "Dual-polarization thin-film lithium niobate in-phase quadrature modulators for terabit-per-second transmission," Optica **9**(1), 61–62 (2022).
22. N. Chen, K. Lou, Y. Yu, *et al.*, "High-efficiency electro-optic modulator on thin-film lithium niobate with high-permittivity cladding," Laser Photonics Rev. **17**(11), 2200927 (2023).
23. X. Meng, C. Yuan, X. Cheng, *et al.*, "Thin-film lithium niobate modulators with ultra-high modulation efficiency," Laser Photonics Rev. **19**(1), 2400809 (2025).
24. X. Guo, Y. Ma, Y. Wang, *et al.*, "Nanowire plasmonic waveguides, circuits and devices," Laser Photonics Rev. **7**(6), 855–881 (2013).
25. A. Tuniz, A. Y. Song, G. Della Valle, *et al.*, "Coupled mode theory for plasmonic couplers," Appl. Phys. Rev. **11**(2), 021309 (2024).
26. M. Alam, J. S. Aitchison, and M. Mojahedi, "Theoretical analysis of hybrid plasmonic waveguide," IEEE J. Sel. Top. Quantum Electron. **19**(3), 4602008 (2013).
27. R. F. Oulton, V. J. Sorger, D. Genov, *et al.*, "A hybrid plasmonic waveguide for subwavelength confinement and long-range propagation," Nat. Photonics **2**(8), 496–500 (2008).
28. A. Tuniz, M. A. Schmidt, and B. T. Kuhlmey, "Influence of non-hermitian mode topology on refractive index sensing with plasmonic waveguides," Photonics Res. **10**(3), 719–730 (2022).
29. W.-P. Huang, "Coupled-mode theory for optical waveguides: an overview," J. Opt. Soc. Am. A **11**(3), 963–983 (1994).
30. H. Chung, W. S. Chang, and E. L. Adler, "Modeling and optimization of traveling-wave linbo/sub 3/interferometric modulators," IEEE J. Quantum Electron. **27**(3), 608–617 (1991).
31. A. Honardoost, R. Safian, A. Rao, *et al.*, "High-speed modeling of ultracompact electrooptic modulators," J. Lightwave Technol. **36**(24), 5893–5902 (2018).
32. Y. Gao, V. Torres-Company, and J. Schröder, "Data accompany 'suppressed hybrid plasmonic mode coupling for efficient electro-optic lithium niobate modulator'," zenodo (2025), https://doi.org/10.5281/zenodo.14961330.